J. Appl. Comput. Mech., xx(x) (2026) 1-18
DOI: 10.22055/jacm.2026.48548.5317

ISSN: 2383-4536
jacm.scu.ac.ir

Shahid Chamran University of Ahvaz

Journal of Applied and Computational Mechanics

Research Paper

Flow Characteristics of Chemically Reactive Magnetohydrodynamic non-Newtonian Fluid with Injection/Suction Effects through Rough Channel

Nasreen Fathima[1], Manjunatha Gudekote[1], Prathiksha Sanil[1], Rajashekhar Choudhari[2], Hanumesh Vaidya[3], Kerehalli Vinayaka Prasad[3]

[1] Department of Mathematics, Manipal Institute of Technology, Manipal Academy of Higher Education, Manipal-576104, India,
Email: nasreen.mitmpl2024@learner.manipal.edu (N.F.); manjunatha.g@manipal.edu (M.G.); sanil.prathiksha@learner.manipal.edu (P.S.)

[2] Department of Mathematics, Manipal Institute of Technology Bengaluru, Manipal Academy of Higher Education, Bengaluru-560063, India, Email: rv.choudhari@manipal.edu

[3] Department of Mathematics, Vijayanagara Sri Krishnadevaraya University, Bellary-583105, India,
Email: hanumeshvaidya@gmail.com (H.V.); prasadkv2007@gmail.com (K.V.P.)

Received June 29 2025; Revised March 31 2026; Accepted for publication April 04 2026.
✉ Corresponding author: M. Gudekote (manjunatha.g@manipal.edu)

Abstract. The present mathematical model investigates the behaviour of magnetohydrodynamic peristaltic transport of non-Newtonian Ree-Eyring fluid in a non-uniform, rough channel embedded within a porous medium. The model is developed by incorporating critical physical phenomena like internal heat generation, wall roughness, slip, and injection/suction effects. The complex interaction of magnetic fields and buoyancy forces with chemical reaction kinetics and thermal gradients is analysed to understand their effects on flow characteristics. The governing nonlinear equations are modelled using the Navier-Stokes equations and are simplified under long wavelength and low Reynolds number regimes. Analytical solutions provide clear insights into the influence of wall roughness, slip, porosity, and electromagnetic forces on the fluid flow characteristics. The graphical outcomes and streamlines obtained using MATLAB R2024b gave a clearer understanding of the flow characteristics in the domain. The magnetohydrodynamic effect provides precise control over fluid flow, while slip and roughness effects cut down the shear stress and energy. The injection/suction mechanism allows regulation of flow rates and removal of products, optimizing chemical reaction efficiency, heat transfer, and mass transport in processes such as polymerization, biochemical reactions, and chemical manufacturing. The current work advances the understanding required for the design of energy efficient, high performance peristaltic transport systems in both industrial and biomedical applications.

Keywords: Ree-Eyring fluid; Injection/suction parameter; Surface roughness; Mixed convection; Slip effects.

1. Introduction

Driven by its broad applicability across physiological processes and industrial systems, the peristaltic mechanism has become a focal point of fluid dynamics research. It refers to a coordinated, rhythmic wall contraction and relaxation of fluid carrying tube/channel which facilitates the transport of material without the need for external pressure gradients. The phenomenon was first observed in biological system, where it played a key role in movement of food waste. However, the study expanded beyond biology when engineers and physicists observed its potential in non-invasive fluid transport system, leading to the development of peristaltic pumps used in medical devices, chemical handling and industrial processes. In modern fluid problems, peristalsis has grown to be a significant field of research, particularly in the modelling of non-Newtonian fluids, microfluidics, and bio-inspired transport mechanisms. Latham's [1] worked on peristaltic transport of viscous fluid, which described the phenomenon of renal pelvis and urethral peristalsis, opened the gateway to study of the peristaltic phenomenon. The research was further carried forward by Shapiro et al. [2], incorporating approximations of large wavelength and lower Reynolds number. The initial investigation considered the fluid to exhibit Newtonian behaviour. However, subsequent studies have demonstrated that most physiological fluids display non-Newtonian behaviour, which in turn lead to study of peristaltic mechanisms involving non-Newtonian factors. The study by Misra and Pandey [3] focused on flow behaviour of power-law fluid flow via a cylindrical tube, incorporating a surrounding additional layer of power-law fluid having distinct viscous characteristics. Hayat et al. [4] focused on heat transfer of MHD viscous fluid that is incompressible in a permeable, asymmetric channel and observed that the heat transfer coefficient was

Published online: April 06 2026

higher in MHD flow than in hydrodynamic fluid flow. More works on peristalsis include [5-7]. Abbasi et al. [8] explored entropy generation and thermal performance of EMHD peristaltic flow of hybrid nanofluid in a two-dimensional asymmetric channel, considering impact of electro-osmosis, hall current, magnetic field.

In several engineering and scientific fields, especially microfluidics, slip flow occurs when the fluid slips along the solid boundary instead of fully sticking, resulting in a non-zero tangential fluid velocity at the wall. This behaviour deviates from the classical no-slip condition and significantly affects flow characteristics near the surface. Rao et al. [9] analysed the peristaltic transport of power-law fluid in an axisymmetric tube with a poroflexible wall pertaining to the application of slip effects. Further study on slip and thermal effects on peristaltic transport of MHD, Newtonian fluid through a porous channel having elastic walls, was investigated by Srinivas et al. [10]. The peristaltic flow of Sutterby fluid within an inclined channel considering the influence of applied magnetic field, with channel walls affected by partial slip conditions, was investigated by Hayat et al. [11]. Tanveer et al. [12] analysed the influence of slip conditions and Joule heating on peristaltic propulsion of Bingham nanofluid in porous channel featuring elastic walls. Results showed that heat transfer rate improved with thermal radiation and thermal slip. Gudekote et al. [13] investigated the influence of magnetohydrodynamics on the peristalsis transport of a non-Newtonian Eyring-Powell fluid with slip effects at the boundary, considering mass and heat transfer within a channel with uniform geometry. Additionally, Sanil et al. [14] conducted a study to examine the influence of chemical reactions in a nonuniform channel, considering temperature-reliant fluid properties on the peristaltic flow of a non-Newtonian Ree-Eyring fluid with slip effects.

The combined effect of chemical reaction, mixed convection and peristalsis is paramount in proper modelling of fluid flow in thermally and chemically active, deformable environments, that finds application in biomedical engineering, industrial processing, and heat and mass transfer systems. The effects of magnetohydrodynamics, chemical reactions, porous media, and peristaltic motion in complex geometries have been widely studied in research [15, 16]. Aliakbarzadeh et al. [17] conducted a numerical investigation of the unsteady mixed convective double-diffusive flow of a water-based nanofluid with a salt species. Nisar et al. [18] considered mixed convective peristaltic flow of chemically sensitive Carreau-Yasuda nanofluid along a porous medium with improved Darcy's law by incorporating slip conditions in a compliant symmetric channel. Yasmin and Nisar [19] studied peristaltic transport under the influence of coupled convection of chemically reacting Casson nanofluid through a symmetrical elastic channel with slip conditions considering the influence of Hall current, and thermal radiation on fluid flow behaviour and heat transfer. A numerical study aimed at the nanofluid flow, emphasizing the combined influences of mixed convection and a surface applied lateral magnetic field was conducted by Behrouz et al. [20]. Subsequently, Nisar et al. [21] studied entropy generation in peristaltic flow of MHD Powell-Eyring nanofluid having deformable channel walls taking into account mixed convection, Hall current, slip conditions, and viscous dissipation. In addition, Berrehal et al. [22] reported a numerical study of the flow, entropy generation, and heat transfer of copper oxide-silver hybrid aqueous nanofluid, under magnetic field.

Injection/suction is a significant boundary control technique in fluid dynamics that involves the addition or removal of fluid through a permeable surface. These mechanisms are broadly applied to several engineering and scientific problems to influence the behaviour of fluid flow near the boundaries. Various studies [23-25] have explored the influence of suction and injection on peristaltic transport in porous, permeable channels, showing that these effects significantly alter velocity, pressure rise, and heat transfer characteristics across both Newtonian and non-Newtonian fluids, including Jeffrey, Carreau models, under magnetohydrodynamic and slip boundary conditions. Abbas et al. [26] analysed the influence of magnetic field and chemical reaction on peristaltic transport of a Jeffrey fluid in a porous channel, incorporating the effects of convective boundary conditions with slip. The study by Mansourian et al. [27] inspected nanofluid flow within a porous medium, stressing on the effects of injection/suction and applied magnetic field on fluid characteristics. Vijayakumar and Reddy [28] analysed the effect of suction and injection on peristaltic flow of a Jeffrey nanofluid in a vertical tube, incorporating complete slip effects at the wall. Chakradhar et al. [29] investigated the impact of magnetic field, and vertical suction and injection, on the peristaltic flow of a Williamson fluid through a permeable channel. Sivaranjani and Kavitha [30] examined the impact of slip conditions, magnetic field, with suction and injection on peristaltic transport of a shear-thinning pseudoplastic fluid, highlighting its importance on biomedical and industrial applications.

Defined by variations in length between peaks and valleys on the surface, surface roughness in channels is an important feature affecting fluid behaviour, pressure drop, and heat transfer rate. Zhang et al. [31] carried a detailed analysis of laminar flow and heat transfer in microchannels incorporated with various roughness features. Rana et al. [32] investigated complex wavy roughness effects on electromagnetohydrodynamic flow and thermal behaviour in porous microchannels by analysing effect of variation in wave amplitudes. The peristaltic flow of Williamson nanofluid over a rough surface within a non-uniform channel under an inclined magnetic field, accounting for viscous dissipation and Joule heating, was analysed by Tanveer et al. [33]. Kumar et al. [34] analysed the thermal behaviour of couple stress fluid flow under peristaltic pumping, emphasizing the role of surface roughness and the geometry of the channel.

Modelling the process of peristalsis using non-Newtonian fluid like Ree-Eyring fluid model proposes a more accurate representation of the rheological behaviour of biological fluids and provides deeper understandings into the dynamics of peristaltic flow. The Peristaltic flow of MHD Ree-Eyring fluids has been studied under various effects, including magnetic fields, chemical reactions, nonlinear radiation, slip conditions, and wall compliance in both endoscopic and curved porous channels [35, 36]. Rajashekhar et al. [37] modelled peristaltic flow of Ree-Eyring fluid with variable fluid properties in a compliant channel that is non-uniform. The peristaltic flow of an electrically conducting Ree-Eyring fluid through a non-uniform symmetric porous conduit, incorporating slip conditions, radiative effects, and entropy generation, was examined by Abbas et al. [38]. Sanil et al. [39] formulated a mathematical peristaltic model of Ree-Eyring fluid considering thermal-dependent variable fluid properties in an axisymmetric, inclined, porous channel by analysing impacts of convective conditions, and chemical reactions, offering insights into fluid behaviour relevant to industrial and biological applications.

The current study extends previous work by examining peristaltic flow of Ree-Eyring fluid with a novel emphasis on the combined effects of velocity slip, chemical reaction, mixed convection, injection-suction, and surface roughness factors that have not been simultaneously explored before but these effects are crucial for accurately modelling fluid-wall interactions, heat and mass transfer, and flow through porous media. These features provide more realistic representation of flow dynamics and thermal characteristics of Ree-Eyring fluids, which is crucial in industrial and biomedical applications. Understanding peristalsis in rough surface channels is vital for designing pumping and conveying systems in chemical, pharmaceutical, and food processing industries, where optimizing flow control, idealising energy consumption, and enhancing equipment durability are crucial. The current investigation contributes to the development of advanced microfluidic devices, artificial organs, and drug delivery systems by ensuring precise fluid regulation, improved heat and mass transfer, and reduced maintenance costs, ultimately driving innovation and efficiency in fluid transport technologies across various industries.

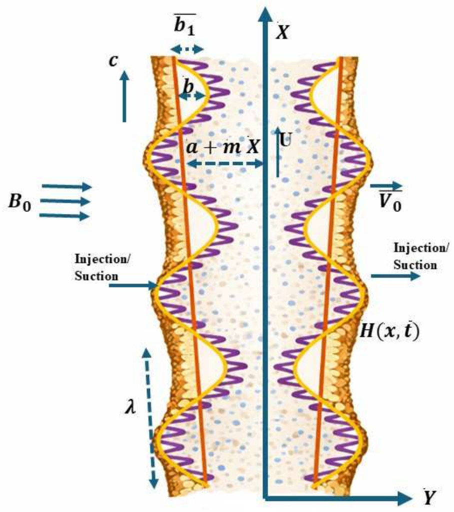

Fig. 1. Schematic illustration of magnetohydrodynamic peristaltic transport of a Ree-Eyring fluid in a rough channel embedded in porous medium with injection/suction effects.

2. Mathematical Formulations

The study investigates the movement of viscous incompressible fluid passing through a non-uniform channel bounded by compliant rough walls. The peristaltic transport mechanism is represented by sinusoidal wave propagation with fluid behaviour described using non-Newtonian Ree-Eyring fluid model. Injection/suction effects are incorporated at the boundary of the channel, wherein fluid injection is carried out perpendicularly to the fluid flow at the lower wall, while suction is imposed at the upper wall (see Fig. 1).

The deformation of the channel walls induced by peristaltic motion over a rough surface is given by [33]:

$$\overline{H}(\overline{X},\overline{t}) = \overline{a} + \overline{m}\overline{X} + \overline{b}\,\cos\left(\frac{2\pi(\overline{X}-c\overline{t})}{\lambda}\right) - \overline{b}_1\cos^4\left(\frac{\pi\overline{X}}{\overline{\lambda}_1}\right). \tag{1}$$

The channel is assumed to be embedded in a porous medium, allowing interaction between the fluid and solid matrix. Peristaltic waves along the rough compliant walls drive the flow, while the applied magnetic field induces Lorentz forces that modify the velocity distribution. Wall roughness and slip conditions account for realistic surface and micro-scale effects. Additionally, internal heat generation and thermal gradients are induced to study heat transfer within the flow domain.

The present configuration is relevant to a wide spectrum of engineering and biomedical systems, including peristaltic pumping devices, microfluidic transport systems, and chemical processing units. The combined effects of magnetic field control, porous medium, and injection/suction mechanisms enable efficient regulation of fluid flow, heat transfer, and mass transport. Such features are particularly useful in polymer processing, biomedical reactors, and targeted drug delivery systems, where precise modulation of transport phenomenon is essential.

Based on the physical configuration illustrated in Fig. 1, the governing equations for the fluid flow in a fixed frame are formulated as:

$$\frac{\partial\overline{U}}{\partial\overline{X}} + \frac{\partial\overline{V_0}}{\partial\overline{Y}} = 0, \tag{2}$$

$$\rho\left(\frac{\partial\overline{U}}{\partial\overline{t}} + \overline{U}\frac{\partial\overline{U}}{\partial\overline{X}} + \overline{V_0}\frac{\partial\overline{U}}{\partial\overline{Y}}\right) = -\frac{\partial\overline{P}}{\partial\overline{X}} + \frac{\partial\overline{\tau}_{\overline{XX}}}{\partial\overline{X}} + \frac{\partial\overline{\tau}_{\overline{XY}}}{\partial\overline{Y}} - \sigma^* B_0^2\overline{U} - \frac{\mu\ \phi^*}{k^*}\overline{U} + \rho g\beta_t(\overline{T}-T_0) + \rho g\beta_c(\overline{C}-C_0), \tag{3}$$

$$\rho\left(\frac{\partial\overline{V_0}}{\partial\overline{t}} + \overline{U}\frac{\partial\overline{V_0}}{\partial\overline{X}} + \overline{V_0}\frac{\partial\overline{V_0}}{\partial\overline{Y}}\right) = -\frac{\partial\overline{P}}{\partial\overline{Y}} + \frac{\partial\overline{\tau}_{\overline{XY}}}{\partial\overline{X}} + \frac{\partial\overline{\tau}_{\overline{YY}}}{\partial\overline{Y}} - \frac{\mu\ \phi^*}{k^*}\overline{V_0}, \tag{4}$$

$$\rho c_p\left(\frac{\partial\overline{T}}{\partial\overline{t}} + \overline{U}\frac{\partial\overline{T}}{\partial\overline{X}} + \overline{V_0}\frac{\partial\overline{T}}{\partial\overline{Y}}\right) = K\left(\frac{\partial^2\overline{T}}{\partial\overline{X}^2} + \frac{\partial^2\overline{T}}{\partial\overline{Y}^2}\right) + Q_0, \tag{5}$$

$$\left(\frac{\partial\overline{C}}{\partial\overline{t}} + \overline{U}\frac{\partial\overline{C}}{\partial\overline{X}} + \overline{V_0}\frac{\partial\overline{C}}{\partial\overline{Y}}\right) = D_m\left(\frac{\partial^2\overline{C}}{\partial\overline{X}^2} + \frac{\partial^2\overline{C}}{\partial\overline{Y}^2}\right) - k_c(\overline{C}-C_0), \tag{6}$$

The constitutive equation describing the stress-strain relation of Ree-Eyring model can be expressed as [39]:

$$\overline{\tau}_{ij} = \mu\frac{\partial\overline{V}_i}{\partial\overline{Y}_j} + \frac{1}{B}\mathrm{Sinh}^{-1}\left(\frac{1}{B_1}\frac{\partial\overline{V}_i}{\partial\overline{Y}_j}\right). \tag{7}$$

Since $\mathrm{Sinh}^{-1}\,\overline{x} \approx \overline{x}$ for $|\overline{x}| \le 1$, then:

$$\overline{\tau}_{ij} = \mu\frac{\partial\overline{V}_i}{\partial\overline{Y}_j} + \frac{1}{B}\left(\frac{1}{B_1}\frac{\partial\overline{V}_i}{\partial\overline{Y}_j}\right). \tag{8}$$

Also, $\overline{V_i} = (\overline{U}, \overline{V})$ and $\overline{x_j} = (\overline{X}, \overline{Y})$. If the wave frame $(\overline{x}, \overline{y})$ comprises of velocity components, $(\overline{u}, \overline{v})$ then:

$$\begin{gathered} \overline{y} = \overline{Y}, \qquad \overline{x} = -c\overline{t} + \overline{X}, \qquad \overline{u}(\overline{x}, \overline{y}) = -c + \overline{U}(\overline{X}, \overline{Y}, \overline{t}), \qquad \overline{v}_0(\overline{x}, \overline{y}) = \overline{V}_0(\overline{X}, \overline{Y}, \overline{t}), \\ \overline{p}(\overline{x}, \overline{y}) = \overline{P}(\overline{X}, \overline{Y}\ , \overline{t}), \qquad \overline{T}(\overline{x}, \overline{y}) = \overline{T}(\overline{X}, \overline{Y}\ , \overline{t}), \qquad \overline{C}(\overline{x}, \overline{y}) = \overline{C}(\overline{X}, \overline{Y}\ , \overline{t}). \end{gathered} \tag{9}$$

The corresponding non-dimensional quantities are:

$$\begin{gathered} x = \frac{\overline{x}}{\lambda}, y = \frac{\overline{y}}{\overline{a}}, t = \frac{c\overline{t}}{\lambda}, \delta = \frac{\overline{a}}{\lambda}, u = \frac{\overline{u}}{c}, v_0 = \frac{\overline{v}_0}{c}, \sigma = \frac{\overline{C} - C_0}{C_1 - C_0}, \theta = \frac{\overline{T} - T_0}{T_1 - T_0}, \epsilon = \frac{\overline{b}}{\overline{a}}, \phi = \frac{\overline{b}_1}{\overline{a}}, m = \frac{\overline{m}}{\overline{a}},\ \lambda_1 = \frac{\overline{\lambda_1}}{\lambda}, Da = \frac{k^*}{\overline{a}^2}, \\ \eta = \frac{1}{\mu \overline{B} B_1}, Re = \frac{\rho c \overline{a}}{\mu},\ M = B_0 \overline{a} \sqrt{\frac{\sigma^*}{\mu}},\ p = \frac{\overline{a}^2 \overline{p}}{\mu\ c},\ \tau_{ij} = \frac{\overline{a}}{\mu\ c} \overline{\tau}_{ij}, \gamma = \frac{k_c \overline{a}^2}{\nu}, B = \frac{Q_0 \overline{a}^2}{\nu (T_1 - T_0)}, Pr = \frac{\mu\ c_p}{K}, Gr = \frac{\rho g \beta_t (\ T_1 - T_0) \overline{a}^2}{\mu\ c}, \\ Sc = \frac{\mu}{\rho D}, Gc = \frac{\rho g \beta_c\ (C_1 - C_0) \overline{a}^2}{\mu\ c}. \end{gathered} \tag{10}$$

Substituting Eq. (9) and Eq. (10) into the set of Eqs. (1)-(6), the following intermediate form of governing equations is obtained:

$$h = 1 + mx + \epsilon\ \cos\big(2\pi(x - t)\big) - \phi\ \left[\cos^4\ \left(\frac{\pi x}{\lambda_1}\right)\right], \tag{11}$$

$$\delta \frac{\partial u}{\partial x} + \frac{\partial v_0}{\partial y} = 0, \tag{12}$$

$$Re \left(\delta u \frac{\partial u}{\partial x} + v_0 \frac{\partial u}{\partial y}\right) = -\frac{\partial p}{\partial x} + \frac{\partial \tau_{xy}}{\partial y} + \delta \frac{\partial \tau_{xx}}{\partial x} - (u+1) M^2 - \frac{1}{Da}(u+1) + Gr\theta + Gc\sigma, \tag{13}$$

$$\delta^3 Re u \frac{\partial v_0}{\partial x} + \delta^2 Re v_0 \frac{\partial v_0}{\partial y} = -\frac{\partial p}{\partial y} + \delta \frac{\partial \tau_{xy}}{\partial y} + \delta^2 \frac{\partial \tau_{xx}}{\partial x} - \frac{\delta^2\ v_0}{D_a}, \tag{14}$$

$$Re \left(\delta (u+1) \frac{\partial \theta}{\partial x} + v_0 \frac{\partial \theta}{\partial y}\right) = \frac{1}{Pr}\left(\delta^2 \frac{\partial^2 \theta}{\partial x^2} + \frac{\partial^2 \theta}{\partial y^2}\right) + B, \tag{15}$$

$$Re \left(\delta (u+1) \frac{\partial \sigma}{\partial x} + v_0 \frac{\partial \sigma}{\partial y}\right) = \frac{1}{Sc}\left(\delta^2 \frac{\partial^2 \sigma}{\partial x^2} + \frac{\partial^2 \sigma}{\partial y^2}\right) - \gamma \sigma. \tag{16}$$

Since the fluid flow is assumed as continuous, steady, and laminar, long-wavelength and lower Reynolds number assumptions are adopted in simplifying the analysis. Consequently, the resulting nondimensional form of nonlinear governing Eqs. (13)-(16) can be expressed as:

$$\frac{\partial p}{\partial x} = \frac{\partial \tau_{xy}}{\partial y} - k \frac{\partial u}{\partial y} - \left(M^2 + \frac{1}{Da}\right)(u+1) + Gr\ \theta + Gc\ \sigma, \tag{17}$$

$$\frac{\partial p}{\partial y} = 0, \tag{18}$$

$$\frac{\partial^2 \theta}{\partial y^2} - k Pr \frac{\partial \theta}{\partial y} + B\ Pr\ = 0, \tag{19}$$

$$\frac{\partial^2 \sigma}{\partial y^2} - k Sc \frac{\partial \sigma}{\partial y} - Sc\ \gamma\ \sigma = 0, \tag{20}$$

where $k = Re\ v_0$ is the injection/suction parameter. Also τ_{xy} gives the constitutive equation of Ree-Eyring fluid model as:

$$\tau_{xy} = (1 + \eta) \frac{\partial u}{\partial y}, \tag{21}$$

The dimensionless form of slip boundary conditions is given by [14]:

$$\frac{\partial u}{\partial y} = 0 \quad \text{at} \quad y = 0 \quad \text{and} \quad u + \beta_1 \tau_{xy} = -1 \quad \text{at} \quad y = h, \tag{22}$$

$$\frac{\partial \theta}{\partial y} = 0 \quad \text{at} \quad y = 0 \quad \text{and}\ \theta + \beta_2 \frac{\partial \theta}{\partial y} = 1 \quad \text{at} \quad y = h, \tag{23}$$

$$\frac{\partial \sigma}{\partial y} = 0 \quad \text{at} \quad y = 0 \quad \text{and} \quad \sigma + \beta_3 \frac{\partial \sigma}{\partial y} = 1 \quad \text{at} \quad y = h. \tag{24}$$

The volume flux is given by the equation:

$$q = \int_0^{h(x)} u\ dy. \tag{25}$$

The dimensionless expression for the flow flux is determined as:

$$Q(x,t) = \int_0^{h(x)} \overline{u}\ d\overline{y}\ = \int_0^{h} (u+1)\ dy\ = q + h. \tag{26}$$

The mean flow rate $\bar{Q}$ over a period $T(=\frac{\lambda}{c})$ is expressed as:

$$\bar{Q} = \frac{1}{T}\int_0^T Q\,dt = \int_0^1 (q+h)\,dx = q+1. \tag{27}$$

3. Solution Methodology

On solving Eq. (20) analytically, with respective boundary conditions in Eqs. (24), solution for concentration is obtained as:

$$\sigma(y) = C_3 e^{A_1 y} + C_2 e^{A_2 y}. \tag{28}$$

Similarly, on solving Eq. (19) analytically, with respective boundary conditions in Eq. (23), solution for temperature is obtained as:

$$\theta(y) = C_5 + C_4\left(-y + \frac{e^{kPry}}{kPr}\right). \tag{29}$$

Incorporating Eqs. (21), (28) and (29) in Eq. (17) and solving analytically with respective boundary conditions in Eqs. (22), solution for velocity is obtained as:

$$u(y) = C_6 e^{H_1 y} + C_7 e^{H_2 y} + H_3 e^{A_1 y} + H_4 e^{A_2 y} + H_5 + H_6 y + H_7 e^{kPry} - \frac{P}{N^2}. \tag{30}$$

The volumetric flow rate can be obtained as:

$$Q = -h + H_{14} + H_{15} + H_{16} - H_{17}\frac{P}{N^2}. \tag{31}$$

The pressure gradient $(\frac{dp}{dx})$, obtained by rearranging terms and comparing equations are as follows:

$$P = \frac{dp}{dx} = -\mathrm{N}^2\left(\frac{Q - h + H_{14} + H_{15} + H_{16}}{H_{17}}\right). \tag{32}$$

The dimensionless pressure rise ΔP is given by:

$$\Delta P = \int_0^1 \frac{dp}{dx}\,dx. \tag{33}$$

The dimensionless wall friction force F over a single wavelength is expressed as follows:

$$F = \int_0^1 h^2\left(-\frac{dp}{dx}\right)dx. \tag{34}$$

The constants $A_i, \text{for } i = 1,2,\ C_j, \text{for } j = 1-7$ and $H_k, \text{for } k = 1-17$ are provided in the appendix. A supplementary file is provided which shows the detailed steps in obtaining the solution.

4. Results and Discussion

The current section aims to analyse the impact of different physical constraints, such as the amplitude ratio (ϵ), non-uniform parameter (m), roughness height (ϕ), Ree-Eyring fluid parameter (η), Magnetic parameter (M), permeability parameter (Da), injection/suction parameter (k), chemical reaction parameter (γ), Schmidt number (Sc), velocity slip parameter (β_1), thermal slip parameter (β_2), concentration slip parameter (β_3), heat-generating parameter (B), Grashof number (Gr), Prandtl number (Pr), modified Grashof number (Gc) and flow rate (Q) on the temperature, concentration, and velocity profiles as illustrated in Figs. 3 to 5, while Figs. 6 to 8 depict the variations in pressure gradient, pressure rise, and frictional force, and Figs. 9-12 present the corresponding streamline patterns. Numerical evaluations are carried out using MATLAB R2024b, which enabled to obtain insight into graphical results and generate streamlines, helping in analysing flow characteristics under different geometrical and flow conditions.

4.1. Validation

Figure 2 illustrates the validation of the present model by comparing its outcomes with those reported by Abbas et al. [26]. To ensure equivalence, the parameters corresponding to the Grashof number, modified Grashof number, porous parameter, Ree-Eyring parameter, and surface roughness height were set to zero, thereby aligning the current formulation with the Newtonian limit adopted to Abbas et al. [26]. Furthermore, no-slip boundary conditions for temperature and concentration were incorporated to maintain consistency between the two models. The resulting comparison exhibits excellent agreement, reinforcing the accuracy and robustness of the proposed mathematical model.

4.2. Temperature profiles

Temperature profiles describe variation in thermal behaviour under varying flow and boundary conditions that are essential for understanding heat transfer characteristics. Numerous physiological factors have different effects on the distribution of temperature through peristaltic flow pipes as seen in the Figs. 3(a)-3(f). As presented in Fig. 3(a), the increase of heat generation parameter elevates fluid temperature, thus, contributing positively to internal thermal energy of the system. The ascension of temperature due to the rise in injection/suction parameter is displayed in Fig. 3(b), which in turn points out heat build-up because the injected fluid brings along thermal energy and gets heat from the system.

The temperature profile, according to Fig. 3(c), is elevated by a larger thermal slip parameter, because of lower thermal resistance at the wall, more heat is thus retained close to the boundary. The raised heat level due to a higher Prandtl number is illustrated in Fig. 3(d) through the decreased thermal diffusivity that prevents heat dispersion and thus leads to thermal accumulation. The influence of channel non-uniformity represented in Fig. 3(e) shows that the growth in non-uniformity parameter leads to temperature increase by changing fluid flow dynamics, prolonging the fluid residency time, thereby resulting in heat retention. Also, as shown in Fig. 3(f), increased roughness height reduces the temperature due to the enhanced mixing of the fluid and disturbance of thermal boundary layer close to the surface, thus more efficient convective heat transfer and dissipation of heat from the surface occur. The eddies formed in the vicinity of the wall, along with the surface irregularity, contribute to the thinning of thermal boundary layer which in turn results in more efficient heat removal and thus, lower temperature.

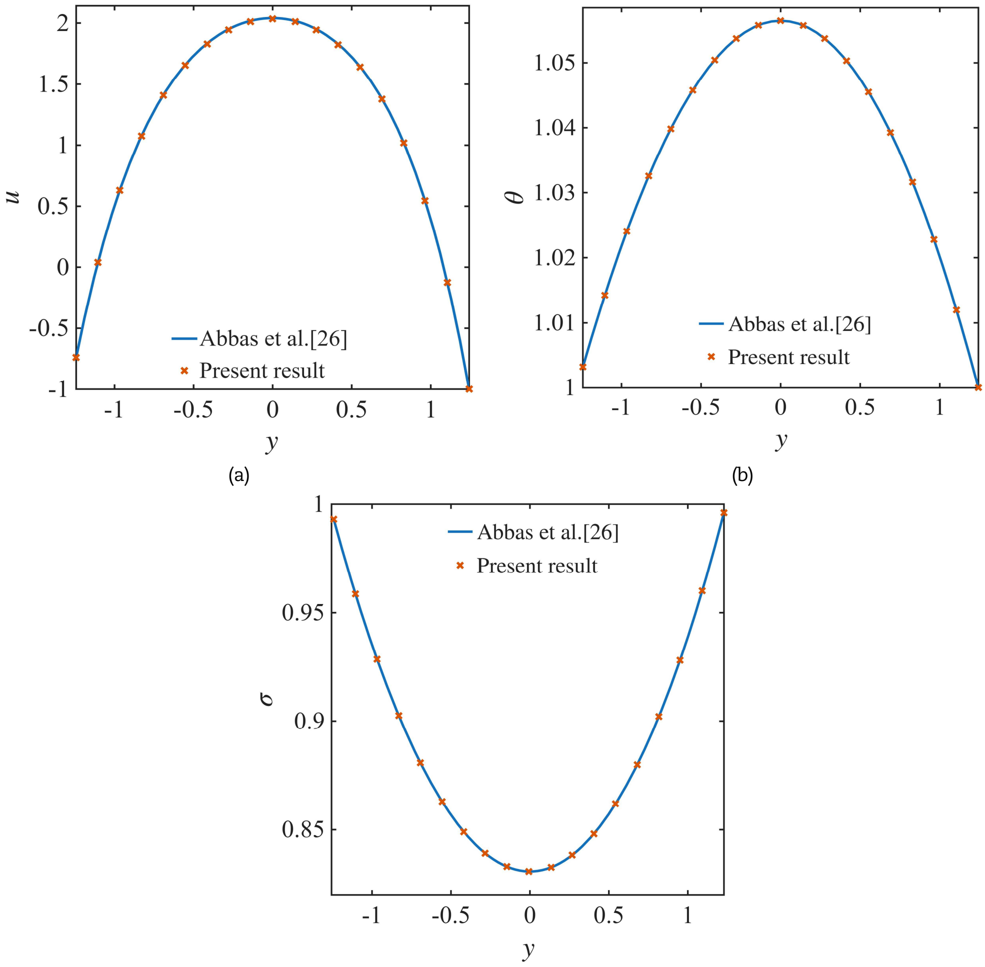

Fig. 2. Validation of the current model against results by Abbas et al. [26] when $Gr = 0, Gc = 0, \ \eta = 0, \phi = 0, \frac{1}{Da} \to 0$, for (a) Velocity profile, (b) Temperature profile, and (c) Concentration profile.

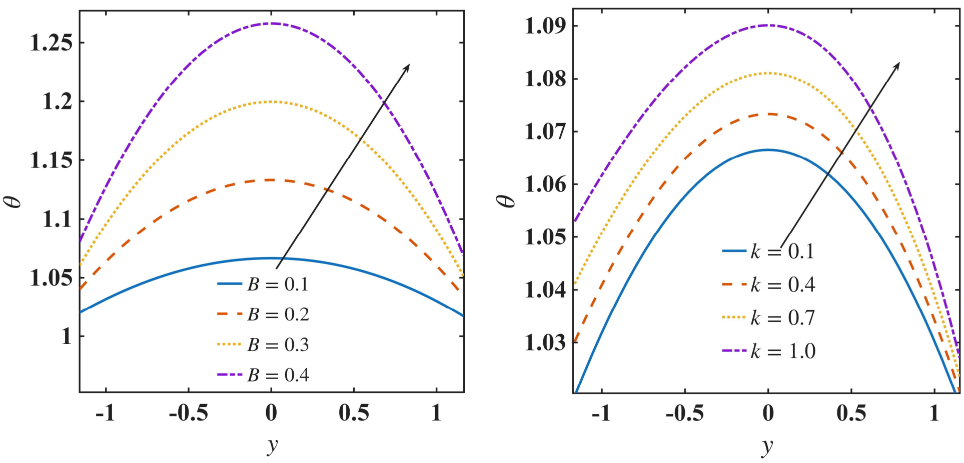

Fig. 3. Variation in temperature profiles when $\epsilon = 0.3, m = 0.2, \phi = 0.1, k = 0.1, \beta_2 = 0.2, B = 0.1, Pr = 0.71$, for (a) Heat generation parameter, (b) Injection/suction parameter, (c) Thermal slip parameter, (d) Prandtl number, (e) non-uniform parameter, (f) Roughness height.

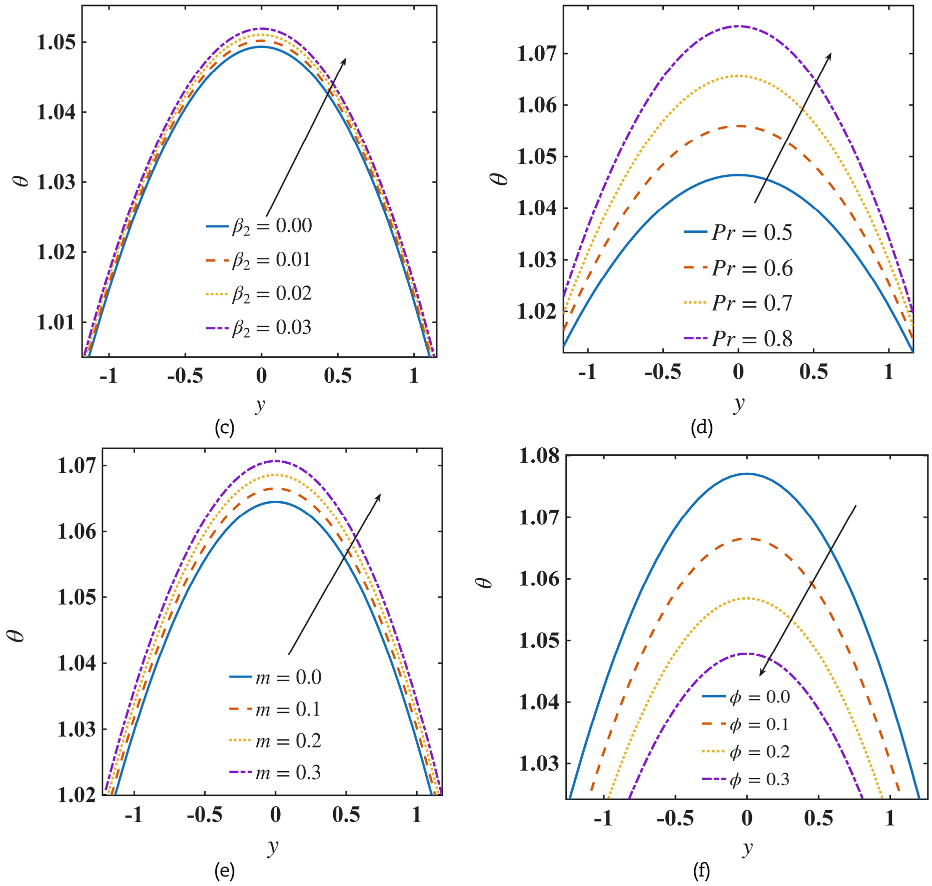

Fig. 3. Continued.

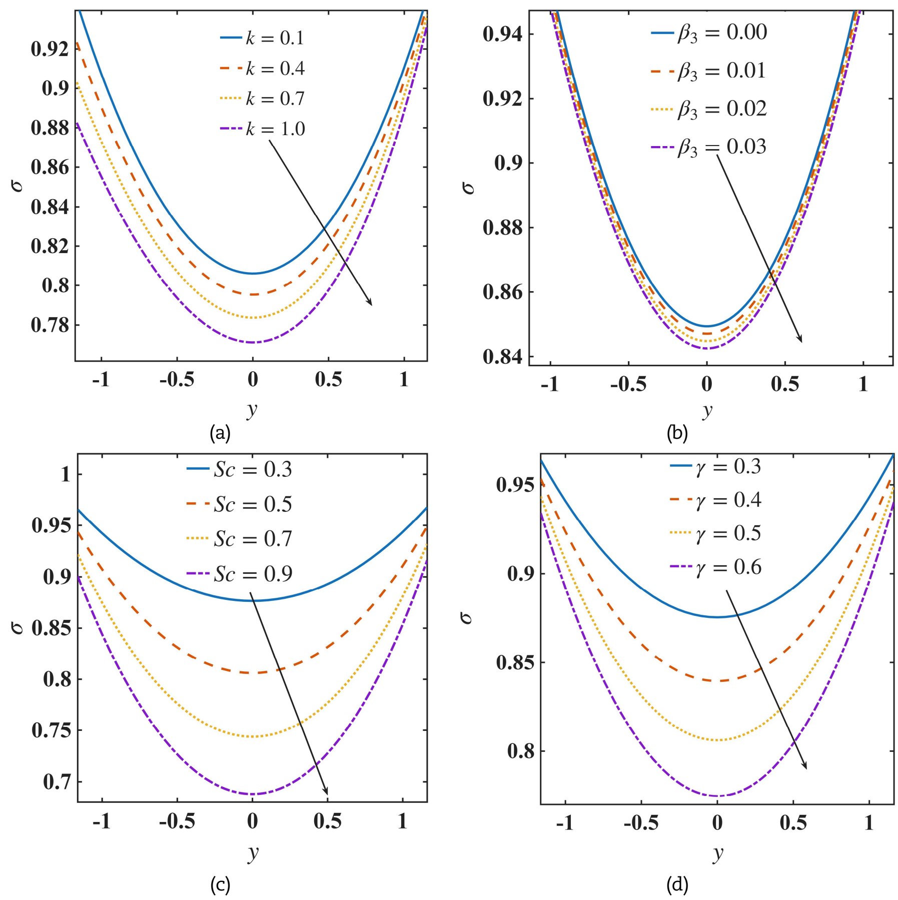

Fig. 4. Variation in concentration profiles when $\epsilon = 0.3$, $m = 0.2$, $\phi = 0.1$, $k = 0.1$, $Sc = 0.5$, $\gamma = 0.5$, $\beta_3 = 0.2$, for (a) Injection/suction parameter, (b) Concentration slip parameter (c) Schmidt number, (d) Chemical reaction parameter, (e) non-uniform parameter, (f) Roughness height.

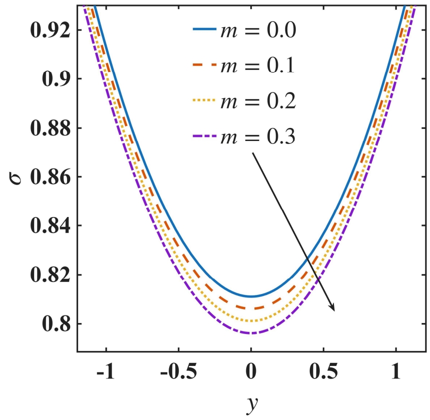

(e)

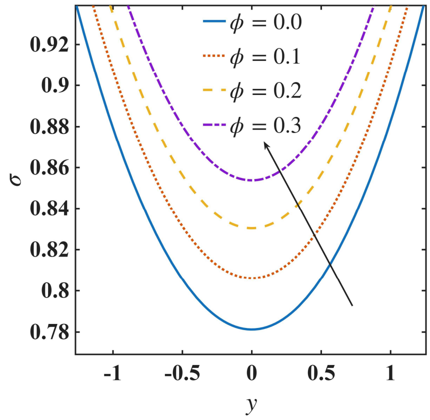

(f)

Fig. 4. Continued.

4.3. Concentration profiles

Concentration profiles are significant in analysing mass transfer phenomena as they depict the spatial arrangement of dissolved particles in the liquid area. The concentrations of the solute in relation to the key governing factors are illustrated in Figs. 4(a)-4(f); these figures reveal a better understanding of mass transfer characteristics of the flow. The figures show that the concentration profiles for the factors concerned are opposite to that of temperature distribution as heat and mass are known to have an inverse relationship. Figure 4(a) indicates that solute concentration within the fluid is decreased by the introduction of injection/suction at the channel boundaries. This is because the mixing of the fluids at the walls enhances the convective mass transport that causes the concentration to not build up. Similarly, Fig. 4(b) indicates that increase in concentration slip parameter results in a drop in concentration since the reduced friction at the wall changes the near wall flow structure and solute retention is decreased. Also, the higher values of Schmidt number and chemical reaction parameter lead to a decline in concentration as shown in Fig. 4(c) and Fig. 4(d), respectively. An increase in Schmidt number indicates lower mass diffusivity, which restrains the solute movement, while faster chemical reactions consuming the solute leave behind a lesser concentration, both of which support the case for the lower concentration profile. Figure 4(e) shows that, for elevated value of non-uniform parameter, the concentration is lowered because the solute transport dynamics are disrupted in a geometrically varying channel. Contrary to this, it can be seen from Fig. 4(f) that as surface roughness height is increased, the mixing near the wall is enhanced which in turn aids in the transport of solute towards the surface and eventually leads to an increase in local concentration.

4.4. Velocity profiles

Analysis of velocity constitutes a fundamental approach to comprehending transport phenomena, enabling the optimization and prediction of fluid transport system performance across biomedical, industrial, and geophysical applications. Various physical and geometric parameters that influence the velocity distribution in a peristaltic channel are discussed below with their sensitivity to fluid properties, thermal conditions, magnetic fields and boundary characteristics. From Fig. 5(a), it can be concluded that the rise in Ree-Eyring fluid parameter causes fluid velocity to fall. This is a typical behaviour of non-Newtonian fluids exhibiting shear thinning, where larger values of this parameter denote a greater resistance to deformation thus yielding less fluid motion. A similar pattern can be seen in Fig. 5(b) where a further rise in the injection/suction parameter results in reduction of velocity profile. This trend is explained by disturbance in the axial momentum balance resulting from the wall-normal mass flux, which modifies the flow field and subsequently diminishes the axial fluid acceleration. The rise in the magnetic field parameter as shown in Fig. 5(c), is correlated with an increase in fluid velocity, which conforms to the findings of Sivaranjani and Kavitha [29]. In general, magnetic fields apply retarding Lorentz force on electrically conducting fluids, however in this particular setup the applied transverse magnetic field combines beneficially with the injection/suction effects and the shape of the channel to give rise to a faster fluid velocity. According to Fig. 5(d), there is a negative correlation between the porous parameter and velocity. In other words, high porous resistance leads to the constriction of flow to narrower areas, thereby increasing local fluid motion. Meanwhile, Fig. 5(e) discusses the effect of heat generation, stating that it not only raises the fluid temperature but also decreases viscosity, ultimately resulting in faster fluid flow. Analogously, Fig. 5(f) suggests that a higher Prandtl number corresponds to a higher fluid speed. A higher Prandtl number implies a lower thermal diffusivity which then creates larger thermal gradients that in turn increase flow momentum. However, in contrast to that, Figs. 5(g)-5(h) show that the increasing of the Schmidt number and chemical reaction parameter reduces velocity. As these parameters are associated with mass transfer and chemical activity, their higher values probably increase the drag due to diffusion or resistance effects, thus lowering the flow velocity. The Grashof number in Fig. 5(i) demonstrates the relationship between the buoyancy forces and fluid motion; thus, the latter is quicker when the former is stronger. Moreover, the slip condition has its impact on shear resistance and makes the flow even at the boundary smoother; thus, the flow is higher with higher slip effect as shown in Fig. 5(k). Figure 5(l) reveals that the rise in the supplied flow rate leads to a proportionate increase in velocity, which is predictable based on the laws of momentum and continuity. The influence of certain geometrical parameters is exhibited in Figs. 5(m)-5(n). Increasing the non-uniformity parameter results in a reduced flow speed due to the flow resistance caused by cross-sectional variations at the point of flow. Additionally, increased roughness height has a similar effect, raising wall friction and disturbing the flow near the wall.

4.5. Pressure gradient profiles

Pressure gradient, the rate at which pressure varies along the direction of flow, is an important parameter depicted in the graphs of flow analysis to demonstrate variation of pressure with varying governing parameters. Figure 6(a) indicates that pressure gradient increases with increased values of the Ree-Eyring fluid parameter. This trend corresponds to increase in resistance to deformation characteristic of non-Newtonian fluids, which requires a higher-pressure gradient to maintain fluid flow. As the magnetohydrodynamic parameter increases, pressure gradient diminishes due to damping action of Lorentz force, that opposes the flow and decreases demand for a sharp pressure gradient after equilibrium is established. Figure 6(b) shows that the injection/suction parameter plays a positive role in the analysis of the pressure gradient. Fluid exchange with the channel walls changes the velocity distribution, making a greater demand on pressure to push the flow.

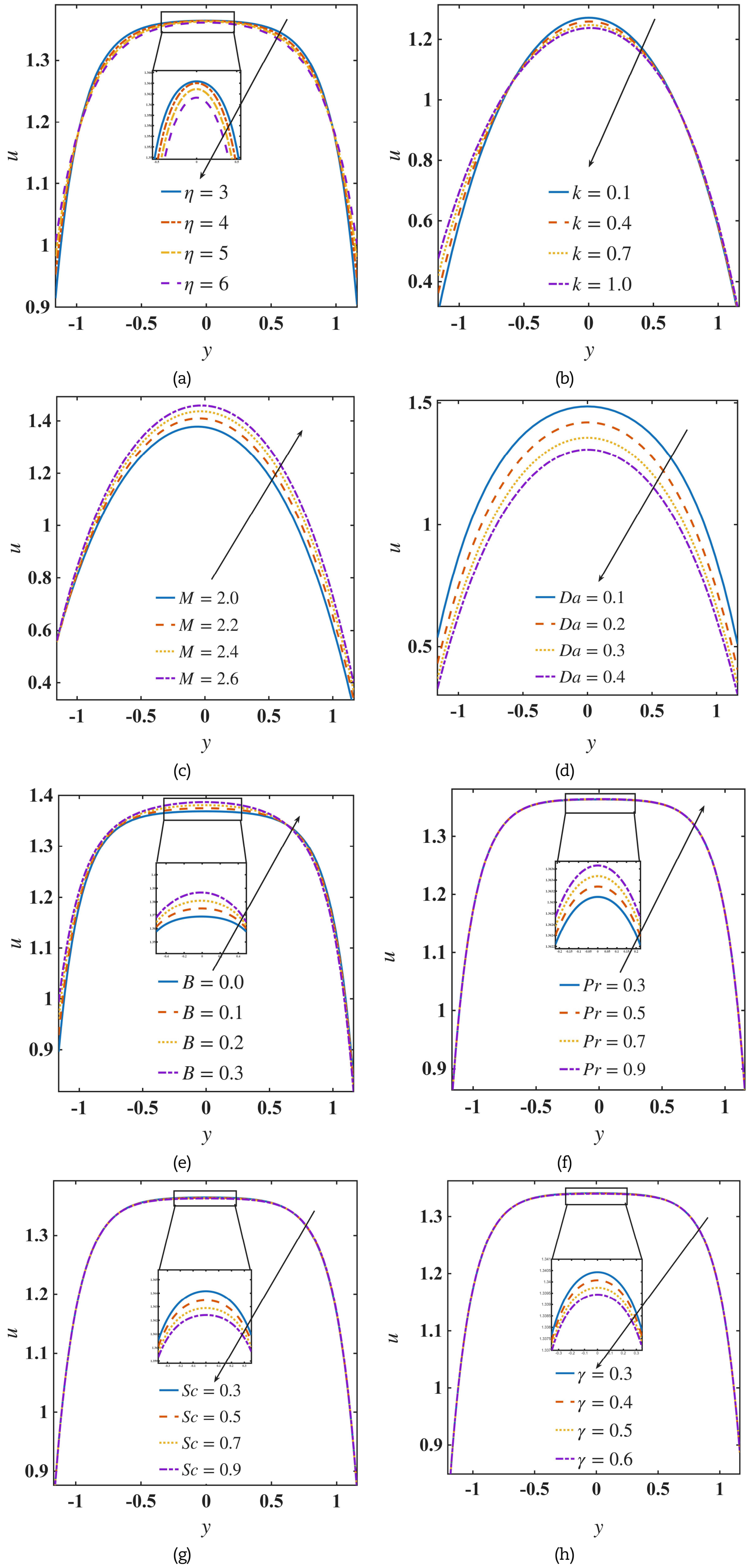

Fig. 5. Variation in velocity profile when $\epsilon = 0.3, m = 0.2, \phi = 0.1, \eta = 2, M = 2, Da = 0.5, k = 0.1, Sc = 0.5, \gamma = 0.5, \beta_1 = \beta_2 = \beta_3 = 0.2, B = 0.1, Gr = 5, Pr = 0.71, Gc = 5, Q = 1.5,$ for (a) Ree-Eyring parameter, (b) Injection/suction parameter, (c) Magnetic parameter, (d) Porous parameter, (e) Heat generation parameter, (f) Prandtl number, (g) Schmidt number, (h) Chemical reaction parameter, (i) Grashof number, (j) Modified Grashof number, (k) Velocity slip parameter, (l) Volumetric flow rate, (m) non-uniform parameter, (n) Roughness height.

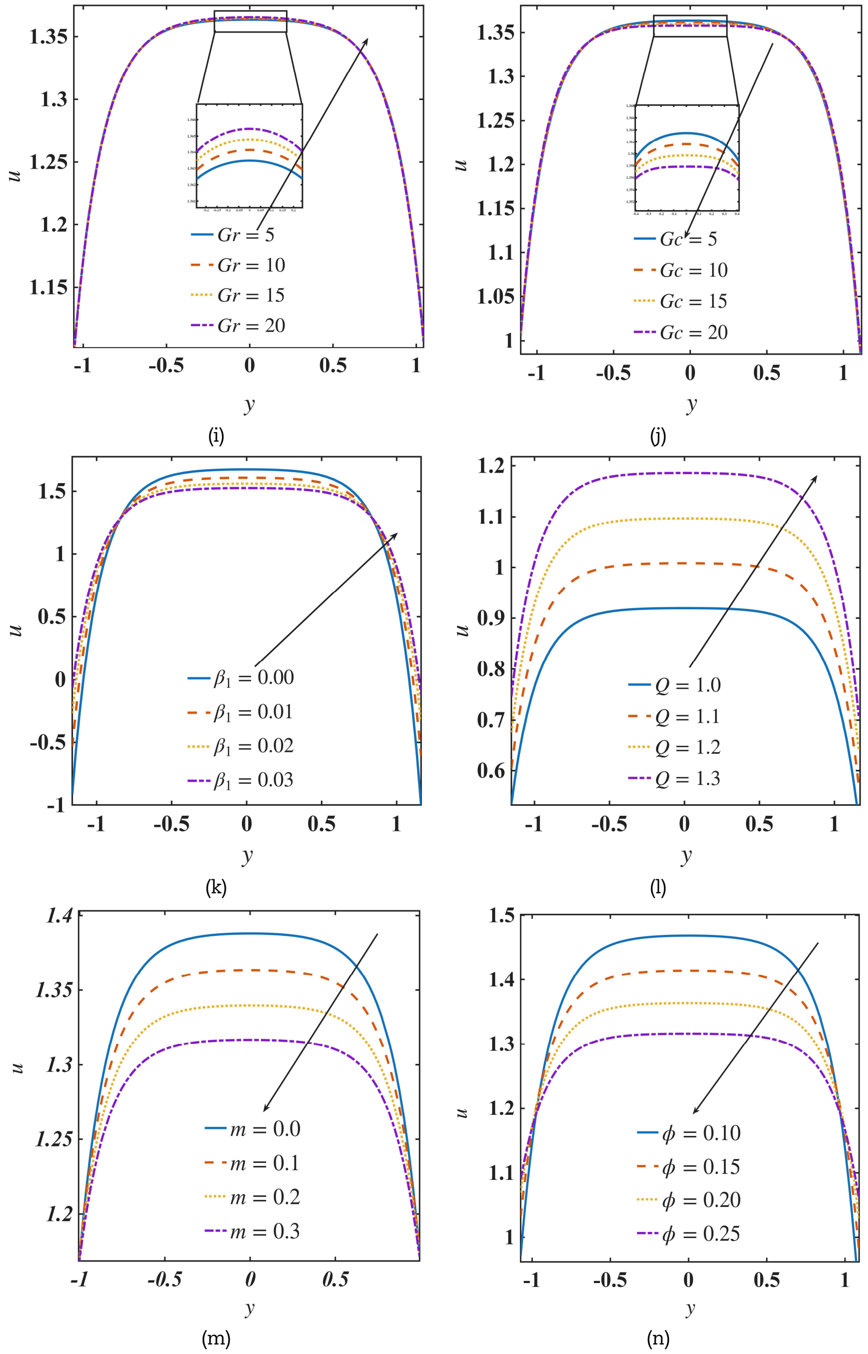

Fig. 5. Continued.

Figures 6(c)-6(d) analyses the impact of magnetic field strength and porous parameter. The magnetic field diminishes the pressure gradient via electromagnetic damping, while the porous parameter has the reverse trend. A higher porosity reflects lesser flow resistance through the porous medium, hence lowering the pressure build-up needed for transport. From Fig. 6(e), a rise in velocity slip leads to elevation in pressure gradient. This occurs since the weakening of shear stress at the wall lowers the exchange of momentum and compels the system to create a stronger pressure field to maintain same flow rate. Figure 6(f) is an illustration of a reverse correlation between pressure gradient and flow rate, where the pressure gradient declines as the flow rate increases, illustrating a more efficient transport mechanism at greater flow volumes. Figure 6(g) illustrates that increasing the non-uniformity parameter has a positive effect on the pressure gradient. Greater axial variation of the channel geometry results in geometric resistance to flow, requiring a higher pressure to maintain flow. However, Fig. 6(h) shows that greater height of the surface roughness leads to lesser pressure gradient. This counter-intuitive phenomenon is due to the perturbation of roughness induced near-wall flow, which reduces resistance by shearing and alters the pressure profile accordingly. The findings collectively provide a complete overview of physical and geometric parameters on pressure gradient in peristaltic flow, which is of very crucial importance for system design optimisation in complicated fluid behaviour applications.

4.6. Pressure rise

Pressure rise is defined as the net pressure rise along flow domain length and is an important parameter in pumping efficiency and flow resistance. The current section illustrates pressure rise variation under the effect of various governing parameters through Figs. 7(a)-(h). The findings demonstrate a clear trend of rising pressure rise with the improvement of each parameter that is under consideration, highlighting their respective contributions to varying resistance and energy dynamics of the flow system.

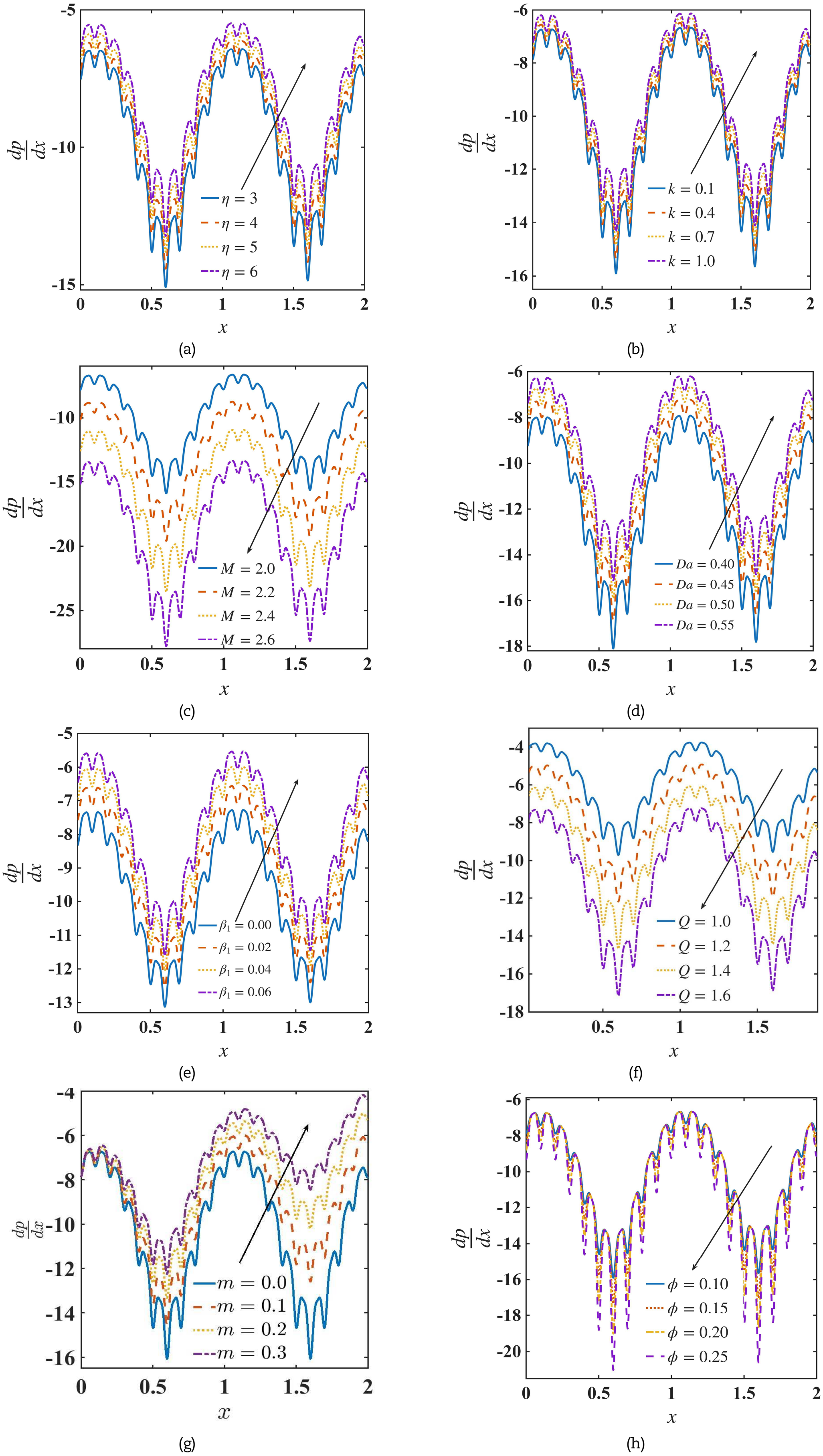

Fig. 6. Variation in pressure gradient when $\epsilon = 0.3, m = 0.2, \phi = 0.1, \eta = 2, M = 2, Da = 0.5, k = 0.1, Sc = 0.5, \gamma = 0.5, \beta_1 = \beta_2 = \beta_3 = 0.2, B = 0.1, Gc = 5, Pr = 0.71, Gr = 5, Q = 1.5$ for (a) Ree-Eyring parameter, (b) Injection/suction parameter, (c) Magnetic parameter, (d) Porous parameter, (e) Velocity slip parameter, (f) Volumetric flow rate (g) non-uniform parameter, (h) Roughness height.

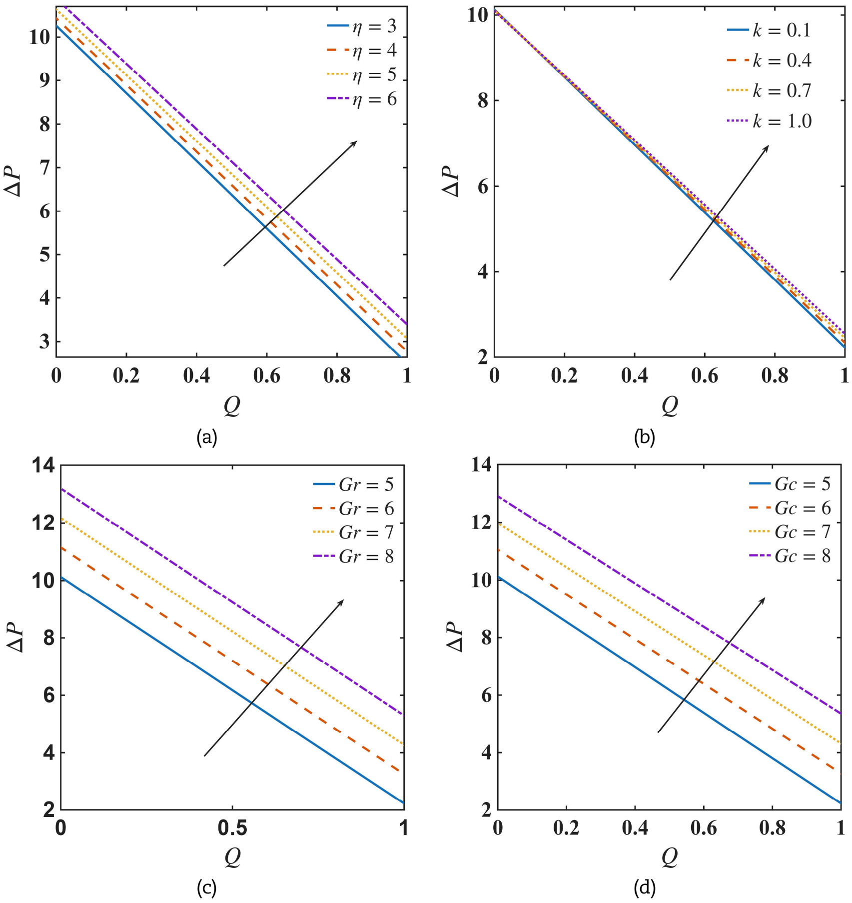

Fig. 7. Variation in pressure-rise when $\epsilon = 0.3, m = 0.2, \phi = 0.1, \eta = 2, M = 2, Da = 0.5, k = 0.1, Sc = 0.5, \gamma = 0.5, \beta_1 = \beta_2 = \beta_3 = 0.2, B = 0.1, Gr = 5, Pr = 0.71, Gc = 5, Q = 1.5$ for (a) Ree-Eyring fluid parameter, (b) Injection/suction parameter, (c) Grashof number, (d) Modified Grashof number.

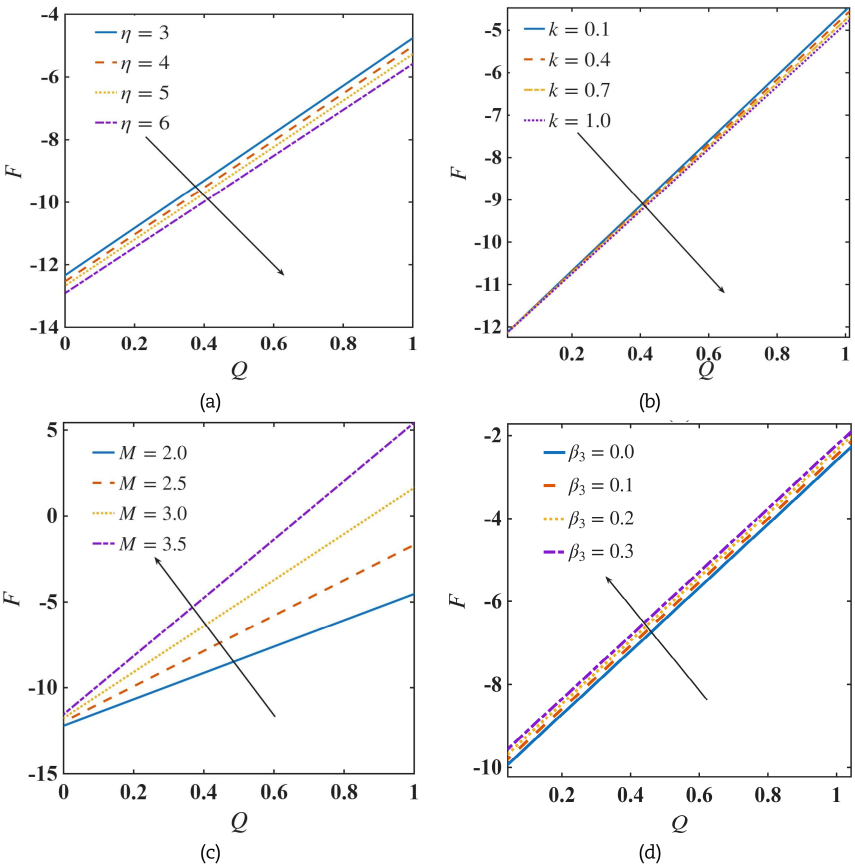

Fig. 8. Variation in friction force when $\epsilon = 0.3, m = 0.2, \phi = 0.1, \eta = 2, M = 2, Da = 0.5, k = 0.1, Sc = 0.5, \gamma = 0.5, \beta_1 = \beta_2 = \beta_3 = 0.2, B = 0.1, Gr = 5, Pr = 0.71, Gc = 5, Q = 1.5$ for (a) Ree-Eyring fluid parameter, (b) Injection/suction parameter, (c) Magnetic parameter, (d) Concentration slip parameter.

Figure 7(a) exhibits that as Ree-Eyring fluid parameter increases, there is a rise in pressure rise. This is due to non-Newtonian character of the fluid, showing that, as the parameter is increased, the fluid demonstrates greater resistance to being deformed and thus needs a higher pressure to sustain the same rate of flow. A similar trend is demonstrated by Fig. 7(b), where the increase in pressure rises with increasing injection/suction parameter. Physically, the existence of wall normal velocity components modifies the axial momentum balance, increased injection tends to resist axial motion, while suction stabilizes it, both effects eventually increase the pressure to maintain the flow. Figures 7(c)-7(d) illustrate the effect of buoyancy forces, characterized by the thermal and solutal Grashof numbers, respectively. In both instances, the rise in these parameters results in an elevation in pressure since stronger buoyancy force-induced convection is combined with the peristaltic pumping mechanism and requires a greater pressure gradient to maintain unidirectional flow.

4.7. Frictional force

Frictional force profiles provide a picture of the distribution of shear force imposed by the fluid on the channel wall and are of considerable significance in understanding wall-fluid interactions. The influence of several parameters on behaviour of frictional force vs. flow rate is described in relation to Figs. 8(a)-8(h). These plots clearly depict the behaviour of frictional force being contrary to pressure variation, implying the complex interface between fluid mechanics and various controlling parameters. Figure 8(a) indicates that, with Ree-Eyring fluid parameter increase, there is a significant reduction in frictional force. Physically, this is due to shear-thinning behaviour of Ree-Eyring fluids, with greater values of the parameter resulting in lower effective viscosity at high shear rates. As a result, the fluid deforms less towards the channel walls and experiences lower wall shear stress and thus lower frictional resistance. Figure 8(b) shows the influence of injection/suction parameter on frictional force. As this parameter is larger, representing higher wall-normal mass flux, there is a decrease in the net friction. This happens because suction at the wall tends towards thinning of boundary layer, reducing shear stress, while injection could reduce the velocity gradient near the wall, both bringing down the friction. The result of magnetohydrodynamic effects is shown in Fig. 8(c). As the MHD parameter increases, frictional force is heightened. This is the direct result of the Lorentz force, a resistive body force that is opposite in direction to the motion of the electrically conducting fluid. Flow velocities are suppressed by the Lorentz force, causing the velocity profile to become steeper near the wall, and hence the shear stress and consequently the frictional force increases. Figure 8(d) illustrates the concentration slip effect. Adding slip at the boundary raises the velocity gradient near the wall. The increased gradient causes a greater mass diffusion rate, which in turn may enhance interfacial stress and thus increase the frictional force.

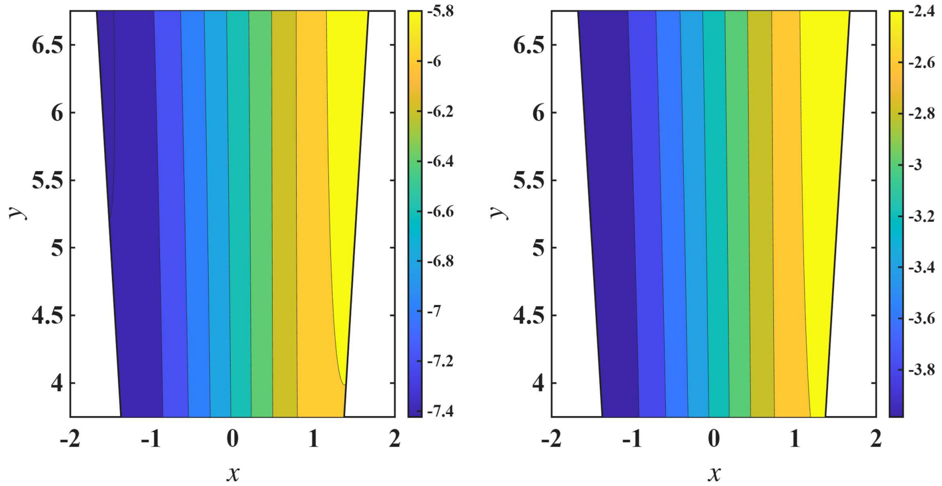

(a) (b)

Fig. 9. Variation in streamline in channel for (a) $k = 0.3$, (b) $k = 0.4$.

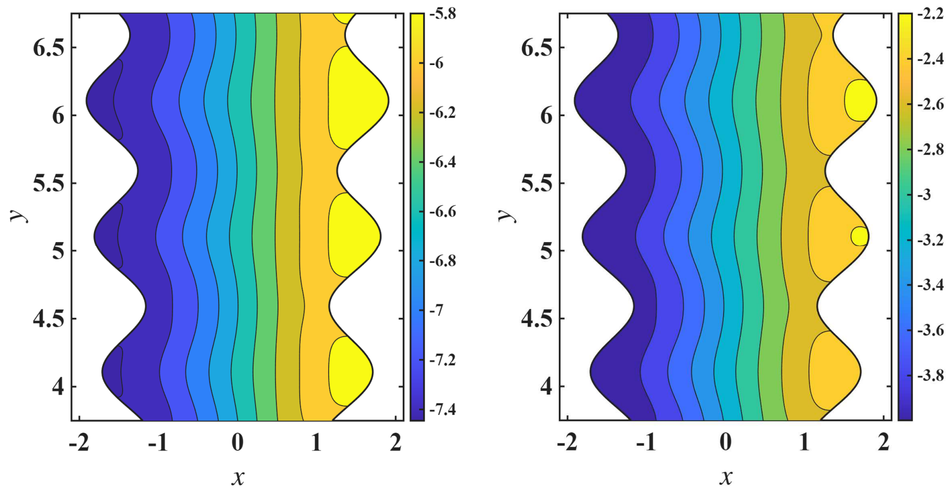

(a) (b)

Fig. 10. Variation in streamline in peristaltic channel for (a) $k = 0.3$, (b) $k = 0.4$.

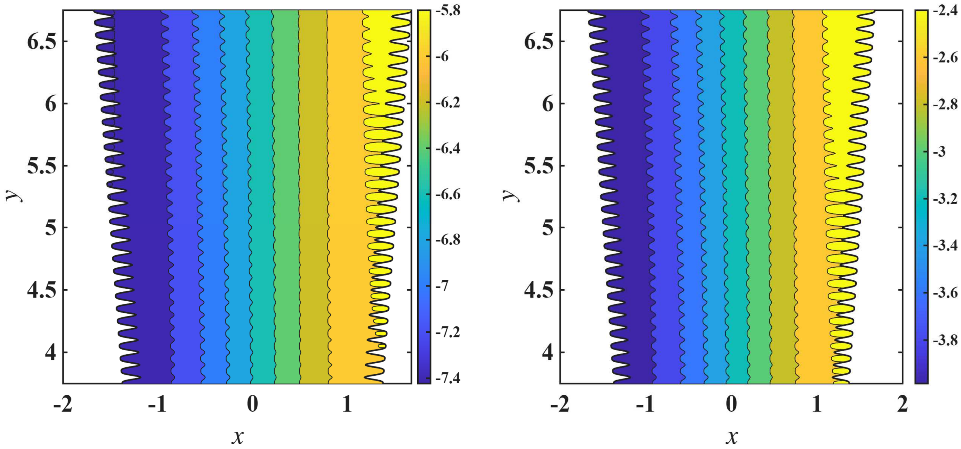

(a) (b)

Fig. 11. Variation in streamline in rough channel for (a) $k = 0.3$, (b) $k = 0.4$.

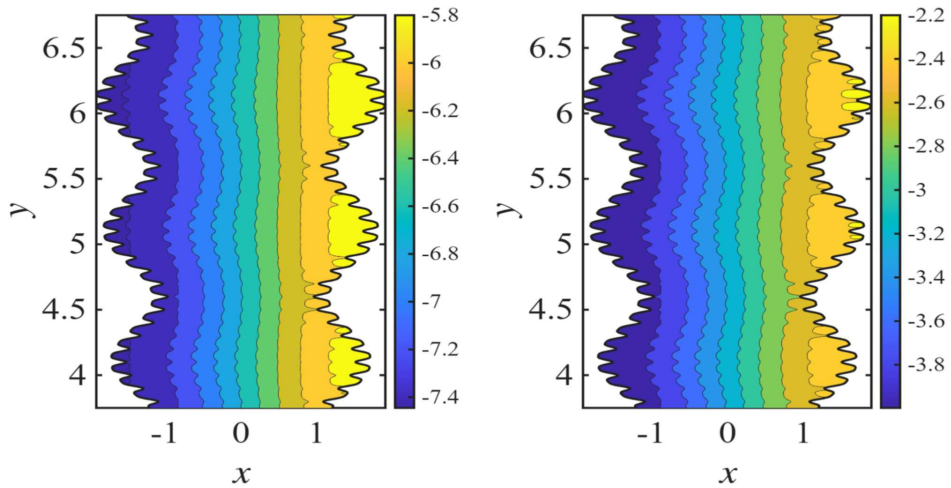

(a) (b)

Fig. 12. Variation in streamline in rough peristaltic channel for (a) $k = 0.3$, (b) $k = 0.4$.

4.8. Stream function

Trapping effects in peristaltic flow are defined as the development of closed streamlines within the fluid region encasing a bolus-a circulating region of fluid which travels with the peristaltic wave without mass exchange with the ambient flow. The contour plots of stream function, pressure, and temperature give an overall insight into the peristaltic transport behaviour under the action of injection/suction and surface roughness. The stream function contours are easily seen to reproduce closed loop structures typical of trapping, with the bolus appearing saliently in central part of the channel and increasing with growing injection strength. The contour plots represented in Figs. 9-12 show the flow behaviour under the influence of varying injection/suction parameters (at $k = 0.3$ and $k = 0.4$). Figure 9 depicts the flow behaviour in normal channel and Fig. 10 represents the flow in peristaltic channel for varying injection/suction parameter. While Fig. 11 represents the variation in rough channel, Fig. 12 depicts the variation in peristaltic channel with rough walls. Increasing the value of the injection/suction parameter makes streamlines in the channel more curved and deviated laterally, reflecting increased transverse motion. This is also evident in the pressure field, whose contours become more oscillatory and entrenched, indicating higher pressure gradients and steeper dynamic changes. The streamline pattern is more compounded and closely packed near the wall for $k = 0.4$, indicating stronger radial disturbances of the flow. Moreover, the surface or wall connected plots show increased amplitude and frequency fluctuations with larger k values, indicative of enhanced wall interactions with possibly an influence on shear and transport properties. Generally, a higher injection/suction parameter yields a more dynamically active flow with greater complexity and stronger near-wall effects.

5. Conclusion

The current model provides valuable insight to analyse the fundamental equations like continuity, momentum and energy and concentration equation which helps in studying the complex rheology of non-Newtonian Ree-Eying fluid model under the effect of wall roughness, slip and injection/section parameters, especially fluid characteristics. The model depicts the analysis of chemical reaction and injection/suction parameter through rough channel. Following are some of the important findings:

- Internal heat generation raises fluid temperature, contributing to heat retention, and injection effect raises temperature by contributing to thermal energy and reduces solute concentration by increasing mixing, important for accurate thermal control and removal of the solute in industrial systems.
- With decreasing thermal diffusivity, heat retention improves. This is especially important for high-viscosity fluids in insulation and food processing applications where retention of heat is vital.
- High surface roughness increases wall mixing, decreasing temperature and enhancing near-wall solute concentration. This is crucial in the design of effective heat exchangers and catalytic reactors for optimal surface interaction.

- Lower mass diffusivity and increased reaction rates decrease the presence of solute in the flow and is used in environmental filtration systems and reactive transport in porous media, for example in pollutant degradation.
- Magnetic effects enhance velocity; greater permeability increases flow. It may be used in MHD pumps and porous filtration devices for fluid control without mechanical components.
- Pressure rise is augmented by internal heat production, slip conditions, and surface roughness factors essential in the design of peristaltic pumps for high-pressure service in biomedical and industrial uses.

The current model efficiently captures complex interactions such as MHD effects, porous wall injection/suction, and wall roughness on non-Newtonian peristaltic flow, offering valuable insights required in bioengineering and industrial applications. It combines chemical reactions, mixed convection, and slip boundary conditions, while maintaining analytical simplicity through long wavelength and low Reynolds number regimes. However, its applicability is limited by neglected inertial forces and three-dimensional effects, confining the model to steady, laminar, and simplified geometries. Future studies can be extended to explore unsteady flows with non-sinusoidal waveforms and three-dimensional channel configurations, while also incorporating numerical simulations to assess solution stability and enhance computational efficiency, thereby providing a more realistic and comprehensive understanding of the problem.

Author Contributions

N. Fathima contributed to the conceptualization, methodology, software and writing of original draft. M. Gudekote contributed to supervision, conceptualization. P. Sanil contributed to modelling and methodology. R. Choudhari conducted the validation. H. Vaidya contributed to investigation. K.V. Prasad contributed to formal analysis. All authors were involved in drafting the manuscript, reviewing the results, and approving the final version.

Acknowledgements

The authors gratefully acknowledge Manipal Academy of Higher Education for extending the essential resources and support to facilitate this investigation.

Conflict of Interest

The authors reported no conflict of interest regarding the authorship or publication of this manuscript.

Funding

The authors declared that no financial support was received for carrying out the research, authorship or publication of this work.

Data Availability Statements

No dataset was generated or analysed during the present study.

Nomenclature

B_0	Magnetic parameter
$\bar{C}$	Concentration
C_0	Fluid concentration at center
C_1	Fluid concentration at wall
c	Wave propagation velocity
C_p	Specific heat at constant volume
D_m	Mass diffusivity coefficient
Da	Permeability parameter
g	Gravitational acceleration
Gc	Modified Grashof number
Gr	Grashof number
H	Non-uniform wave
k	Injection/suction parameter
k^*	Permeability
k_c	Chemical reaction rate
K	Thermal conductivity
M	Magnetic parameter
m	Non-uniform parameter
p	Pressure
Pr	Prandtl number
Q_0	Heat generation parameter
Re	Reynolds number
Sc	Schmidt number
T	Temperature
T_0	Fluid temperature at center
T_1	Fluid temperature at wall
$\bar{t}$	Time
$\bar{U}$	Axial velocity
$\overline{V_0}$	Radial velocity
x	Axial coordinate
y	Radial coordinates

Greek Symbols

β_c	Concentration expansion coefficient
β_t	Thermal expansion coefficient
β_1	Slip parameter for velocity
β_2	Slip parameter for temperature
β_3	Slip parameter for concentration
δ	Wave number
ϵ	Amplitude ratio
γ	Chemical reaction parameter
η	Ree-Eyring parameter
λ	Wavelength
$\overline{\lambda_1}$	Pitch
μ	Constant viscosity
ρ	Fluid density
σ	Concentration
σ^*	Electric conductivity
ϕ	Roughness height
ϕ^*	Porosity of the medium
θ	Dimensionless Temperature
$\bar{\tau}_{ij}$	Components of stress tensor (i,j = x,y)

Subscripts

0	Centre condition
1	Wall condition
c	Concentration-related
t	Thermal-related
w	Wall
m	Mean

Superscripts

*‾	Dimensionless quantity

Appendix

$$A_1 = \frac{kSc - \sqrt{4\gamma Sc + k^2 Sc^2}}{2}, \tag{A.1}$$

$$A_2 = \frac{kSc + \sqrt{4\gamma Sc + k^2 Sc^2}}{2}, \tag{A.2}$$

$$N = \sqrt{M^2 + \frac{1}{Da}}, \tag{A.3}$$

$$R = 1 + \eta, \tag{A.4}$$

$$C_1 = -\frac{A_2}{A_1}, \tag{A.5}$$

$$C_2 = \frac{1}{C_1 e^{A_1 h}(1 + \beta_3 A_1) + e^{A_2 h}(1 + \beta_3 A_2)}, \tag{A.6}$$

$$C_3 = C_1 C_2, \tag{A.7}$$

$$C_4 = -\frac{B}{k}, \tag{A.8}$$

$$C_5 = 1 + C_4(h + \beta_2) - C_4 e^{kPrh}\left(\beta_2 + \frac{1}{kPr}\right), \tag{A.9}$$

$$H_1 = \frac{k - \sqrt{k^2 + 4RN^2}}{2R}, \tag{A.10}$$

$$H_2 = \frac{k + \sqrt{k^2 + 4RN^2}}{2R}, \tag{A.11}$$

$$H_3 = -\frac{GcC_3}{A_1^2 R - A_1 k - N^2}, \tag{A.12}$$

$$H_4 = -\frac{GcC_3}{A_2^2 R - A_2 k - N^2}, \tag{A.13}$$

$$H_5 = \frac{GrkC_4}{N^4} + \frac{GrC_5}{N^2} - 1, \tag{A.14}$$

$$H_6 = -\frac{GrC_4}{N^2}, \tag{A.15}$$

$$H_7 = \frac{GrC_4}{kPr(k^2 Pr(1 - PrR) + N^2)}, \tag{A.16}$$

$$H_8 = H_3 A + H_4 B + H_6 + H_7 kPr, \tag{A.17}$$

$$H_9 = -\frac{H_8}{H_1}, \tag{A.18}$$

$$H_{10} = \frac{H_1}{H_2}, \tag{A.19}$$

$$H_{11} = H_9 e^{H_2 h} + H_3 e^{A_1 h} + H_4 e^{A_2 h} + H_5 + H_6 h + H_7 e^{KPrh}, \tag{A.20}$$

$$H_{12} = H_9 H_2 e^{H_2 h} + H_3 A_1 e^{A_1 h} + H_4 A_2 e^{A_2 h} + H_6 + H_7 kPr e^{kPrh}, \tag{A.21}$$

$$H_{13} = e^{H_1 h} - H_{10} e^{H_2 h} + R\beta_1 \left(H_1 e^{H_1 h} - H_2 H_{10} e^{H_2 h}\right), \tag{A.22}$$

$$H_{14} = \frac{H_3(e^{A_1 h} - 1)}{A_1} + \frac{H_4(e^{A_2 h} - 1)}{A_2} + \frac{H_6 h^2}{2} + H_5 h, \tag{A.23}$$

$$H_{15} = \left(\frac{e^{H_1 h} - 1}{H_1} + H_{10}\frac{e^{H_2 h} - 1}{H_2}\right)\left(\frac{1 + H_{11} + R\beta_1 H_{12}}{H_{13}}\right), \tag{A.24}$$

$$H_{16} = \frac{H_7(e^{kPrh} - 1)}{kPr} + \frac{H_9 e^{H_2 h} - 1}{H_2}, \tag{A.25}$$

$$H_{17} = \frac{H_{10}(e^{H_2 h} - 1)}{H_2 H_{13}} + \frac{e^{H_1 h} - 1}{H_1 H_{13}}, \tag{A.26}$$

$$C_6 = \frac{-1 + \dfrac{P}{N^2} - H_{11} - R\beta_1 H_{12}}{H_{13}}, \tag{A.27}$$

$$C_7 = H_9 - H_{10}C_6. \tag{A.28}$$

References

[1] Latham, T.W., *Fluid Motions in a Peristaltic Pump*, PhD Thesis, Massachusetts Institute of Technology, 1966.
[2] Shapiro, A.H., Jaffrin, M.Y., Weinberg, S.L., Peristaltic Pumping with Long Wavelengths at Low Reynolds Number, *Journal of Flluid Mechanics*, 37(4), 1969, 799-825.
[3] Misra, J.C., Pandey, S.K., Peristaltic Flow of a Multilayered Power-Law Fluid through a Cylindrical Tube, *International Journal of Engineering Science*, 39(4), 2001, 387-402.
[4] Hayat, T., Qureshi, M.U., Hussain, Q., Effect of Heat Transfer on the Peristaltic Flow of an Electrically Conducting Fluid in a Porous Space, *Applied Mathematical Modelling*, 33(4), 2009, 1862-1873.
[5] Hina, S., Mustafa, M., Hayat, T., Alsaadi, F.E., Peristaltic Motion of Third Grade Fluid in Curved Channel, *Applied Mathematics and Mechanics*, 35(1), 2014, 73-84.
[6] Tripathi. D., Jhorar, R., Anwar, B.O., Shaw, S., Electroosmosis Modulated Peristaltic Biorheological Flow through an Asymmetric Microchannel: Mathematical Model, *Meccanica*, 53(8), 2018, 2079-2090.
[7] Asghar, Z., Khan, M.W.S., Gondal, M.A., Ghaffari, A., Channel Flow of Non-Newtonian Fluid Due to Peristalsis Under External Electric and Magnetic Field, *Proceedings of the Institution of Mechanical Engineers, Part E, Journal of Process Mechanical Engineering,* 236(6), 2022, 2670-2678.
[8] Abbasi, F.M., Iqbal, J., Nawaz, R., Analysis of Thermal Characteristics for MHD Peristaltic Movement of Hybrid Nanofluid with Electro-Osmosis, Ohmic Heating and Hall Effects, *International Journal of Heat and Fluid Flow*, 107, 2024, 109405.
[9] Rao, A.R., Mishra, M., Peristaltic Transport of a Power-Law Fluid in a Porous Tube, *Journal of Non-Newtonian Fluid Mechanics*, 121(2-3), 2004, 163-174.
[10] Srinivas, S., Gayathri, R., Kothandapani, M., The Influence of Slip Conditions, Wall Properties and Heat Transfer on MHD Peristaltic Transport, *Computer Physics Communications*, 180(11), 2009, 2115-2122.
[11] Hayat, T., Ayub, S., Tanveer, A., Alsaedi, A., Slip and Joule Heating Effects on Peristaltic Transport in an Inclined Channel, *Journal of Thermal Science and Engineering Applications*, 10(3), 2018, 031004.
[12] Tanveer, A., Khan, M., Salahuddin, T., Malik, M.Y., Numerical Simulation of Electroosmosis Regulated Peristaltic Transport of Bingham Nanofluid, *Computer Methods and Programs in Biomedicine*, 180, 2019, 105005.
[13] Gudekote, M., Choudhari, R., Sanil, P., Hadimani, B., Vaidya, H., Prasad, K.V., MHD Effects on the Peristaltic Transport of Non-Newtonian Eyring-Powell Fluid with Heat and Mass Transfer in an Inclined Uniform Channel, *Arabian Journal for Science and Engineering*, 49(11), 2024, 15143-15159.
[14] Sanil, P., Gudekote, M., Choudhari, R., Madhavi, M.R., Vaidya, H., Prasad, K.V., A Mathematical Approach to the Role of Chemical Reactions and Temperature-Dependent Fluid Properties on the Peristaltic Transport of Non-Newtonian Ree-Eyring Fluid in a Nonuniform Channel, *Discover Applied Sciences*, 7(3), 2025, 199.
[15] Srinivas, S., Muthuraj, R., Effects of Chemical Reaction and Space Porosity on MHD Mixed Convective Flow in a Vertical Asymmetric Channel with Peristalsis, *Mathematical and Computer Modelling*, 54(5-6), 2011, 1213-1227.
[16] Hayat, T., Tanveer, A., Alsaedi, A., Numerical Analysis of Partial Slip on Peristalsis of MHD Jeffery Nanofluid in Curved Channel with Porous Space, *Journal of Molecular Liquids*, 224, 2016, 944-953.
[17] Kashani, D.A., Dinarvand, S., Pop, I., Hayat, T., Effects of Dissolved Solute on Unsteady Double-Diffusive Mixed Convective Flow of a Buongiorno's Two-Component Nonhomogeneous Nanofluid, *International Journal of Numerical Methods for Heat & Fluid Flow*, 29(1), 2019, 448-466.
[18] Nisar, Z., Hayat, T., Alsaedi, A., Momani, S., Peristaltic Flow of Chemically Reactive Carreau-Yasuda Nanofluid with Modified Darcy's Expression, *Materials Today Communications*, 33, 2022, 104532.
[19] Yasmin, H., Nisar, Z., Mathematical Analysis of Mixed Convective Peristaltic Flow for Chemically Reactive Casson Nanofluid, *Mathematics*, 11(12), 2023, 2673.
[20] Behrouz, M., Dinarvand, S., Yazdi, M.E., Tamim, H., Pop, I., Chamkha, A.J., Mass-Based Hybridity Model for Thermomicropolar Binary Nanofluid Flow: First Derivation of Angular Momentum Equation, *Chinese Journal of Physics*, 83, 2023, 165-184.
[21] Nisar, Z., Ahmed, B., Aziz, A., Muhammad, K., Elseesy, I.E., Impacts of Entropy Generation for Nonlinear Radiative Peristaltic Transport of Powell-Eyring Nanofluid: A Numerical Study, *Numerical Heat Transfer, Part A: Applications,* 85(23), 2024, 4114-4132.
[22] Berrehal, H., Karami, R., Dinarvand, S., Pop, I., Chamkha, A., Entropy Generation Analysis for Convective Flow of Aqua Ag-Cuo Hybrid Nanofluid Adjacent to a Warmed Down-Pointing Rotating Vertical Cone, *International Journal of Numerical Methods for Heat & Fluid Flow,* 34(2), 2024, 878-900.
[23] Kavitha, A., Reddy, R.H., Srinivas, A.N., Sreenadh, S., Saravana, R., Peristaltic Pumping of a Jeffrey Fluid Between Porous Walls with Suction and Injection, *International Journal of Mechanical and Materials Engineering,* 7(2), 2012, 152-157.
[24] Sivaiah, R., Reddy, R.H., Magnetohydrodynamic Peristaltic Motion of a Newtonian Fluid Through Porous Walls Through Suction and Injection, *IOP Conference Series: Materials Science and Engineering,* 263(6), 2017, 062007.
[25] Kumari, S.K., Vernekar, D.S., Comparative Study of Effect of Peristalsis with Suction/Injection and Cilia on the Flow of MHD Jeffrey Fluid, *High Technology Letters*, 26(12), 2020, 477-493.
[26] Abbas, Z., Rafiq, M.Y., Hasnain, J., Umer, H., Impacts of Lorentz Force and Chemical Reaction on Peristaltic Transport of Jeffrey Fluid in a Penetrable Channel with Injection/Suction at Walls, *Alexandria Engineering Journal,* 60(1), 2021, 1113-1122.
[27] Mansourian, M., Dinarvand, S., Pop, I., Aqua Cobalt Ferrite/Mn–Zn Ferrite Hybrid Nanofluid Flow Over a Nonlinearly Stretching Permeable Sheet in a Porous Medium, *Journal of Nanofluids,* 11(3), 2022, 383-391.
[28] Vijayakumar, P., Reddy, R.H., Influence of Suction and Injection on Peristaltic Mechanism of a Jeffrey Nanofluid in a Vertical Channel with Complete Slip Effects, *Journal of Nanofluids*, 13(1), 2024, 130-144.
[29] Chakradhar, K., Nandagopal, K., Prashanthi, V., Parandhama, A., Somaiah, T., Thrinath, B.S., Tarakaramu, N., Rasool, G., Abduvalieva, D., MHD Effect on Peristaltic Motion of Williamson Fluid via Porous Channel with Suction and Injection, *Partial Differential Equations in Applied Mathematics*, 13, 2025, 101103.
[30] Sivaranjani, S., Kavitha, A., Impact of First Order Slip Condition on Peristaltic Transport of a Pseudoplastic Fluid Under MHD Effect Bounded by Permeable Walls with Suction and Injection, *Contemporary Mathematics*, 6(1), 2025, 1091-1109.
[31] Zhang, C., Chen, Y., Shi, M., Effects of Roughness Elements on Laminar Flow and Heat Transfer in Microchannels, *Chemical Engineering and Processing: Process Intensification*, 49(11), 2010, 1188-1192.
[32] Rana, A., Reza, M., Shit, G.C., Electromagnetohydrodynamic Thermo-Fluidic Transport in a Porous Microchannel with Wall Roughness, *Colloids and Surfaces A: Physicochemical and Engineering Aspects*, 650, 2022, 129336.

[33] Tanveer, A., Rasheed, I., Jarral, S., Peristaltic Flow of Williamson Nanofluid on a Rough Surface, *Advances in Mechanical Engineering*, 16(1), 2024, 16878132231222793.
[34] Kumar, A., Bhardwaj, A., Tripathi, D., Thermal Analysis in Peristaltic Pumping: Effects of Surface Roughness and Channel Geometries, *Physics of Fluids*, 37(2), 2025, 023122.
[35] Hayat, T., Akram, J., Alsaedi, A., Zahir, H., Endoscopy and Homogeneous-Heterogeneous Reactions in MHD Radiative Peristaltic Activity of Ree-Eyring Fluid, *Results in Physics*, 8, 2018, 481-488.
[36] Tanveer, A., Malik, M.Y., Slip and Porosity Effects on Peristalsis of MHD Ree-Eyring Nanofluid in Curved Geometry, *Ain Shams Engineering Journal*, 12(1), 2021, 955-968.
[37] Choudhari, R., Vaidya, H., Gudekote, M., Dodo, Y.A., Prasad, K.V., Gnaba, H., Amat, R.H., Khan, M.I., Mathematical Modelling and Simulation of Peristaltic Activity in Ree-Eyring Fluid Flow Through Non-Uniform Complaint Channel: Different Varying Conditions, *Journal of the Indian Chemical Society*, 100(3), 2023, 100954.
[38] Abbas, Z., Rafiq, M.Y., Yaqoob, S., Shahzad, H., Entropy Generation Analysis for the Peristaltic Motion of Ree-Eyring Fluid Through a Porous Symmetric Channel Under Slip Constraints, *Proceedings of the Pakistan Academy of Sciences: A. Physical and Computational Sciences*, 62(1), 2025, 21-30.
[39] Sanil, P., Choudhari, R., Gudekote, M., Vaidya, H., Prasad, K.V., Impact of Chemical Reactions and Convective Conditions on Peristaltic Mechanism of Ree-Eyring Fluid in a Porous Medium–A Mathematical Model, *International Journal of Thermofluids*, 26, 2025, 101086.

ORCID iD

Nasreen Fathima https://orcid.org/0009-0005-5387-6190
Manjunatha Gudekote https://orcid.org/0000-0001-5347-753X
Prathiksha Sanil https://orcid.org/0009-0004-0579-5006
Rajashekhar Choudhari https://orcid.org/0000-0001-8950-7104
Hanumesh Vaidya https://orcid.org/0000-0001-5343-8039
Kerehalli Vinayaka Prasad https://orcid.org/0000-0001-6737-1162

How to cite this article: Fathima N., et al., Flow Characteristics of Chemically Reactive Magnetohydrodynamic non-Newtonian Fluid with Injection/Suction Effects through Rough Channel, *J. Appl. Comput. Mech.*, xx(x), 2026, 1–18. https://doi.org/10.22055/jacm.2026.48548.5317